Energy Storage Materials 70 (2024) 103543

Contents lists available at ScienceDirect

Energy Storage Materials

journal homepage: www.elsevier.com/locate/ensm

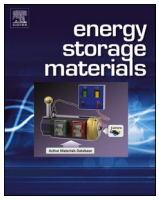

Unlocking plateau capacity with versatile precursor crosslinking for carbon anodes in Na-ion batteries

Xiaobing Zhao [a,b,c,d], Peng Shi [f], Haibo Wang [a,b,d], Qingshi Meng [e], Xingguo Qi [e], Guanjie Ai [a,b], Fei Xie [a], Xiaohui Rong [a,b,d], Ying Xiong [f], Yaxiang Lu [a,b,c,d,*], Yong-Sheng Hu [a,b,c,d,e]

[a] Key Laboratory for Renewable Energy, Beijing Key Laboratory for New Energy Materials and Devices, Beijing National Laboratory for Condensed Matter Physics, Institute of Physics, Chinese Academy of Sciences, Beijing 100190, China
[b] College of Materials Science and Optoelectronic Technology, University of Chinese Academy of Sciences, Beijing 100049, China
[c] Huairou Division, Institute of Physics, Chinese Academy of Sciences, Beijing 101400, China
[d] Yangtze River Delta Physics Research Center Co., Ltd., Liyang 213300, China
[e] HiNa Battery Technology Co., Ltd., Beijing, China
[f] College of Chemistry, Liaoning University, Shenyang 110036, China

ARTICLE INFO

Keywords:
Precursor crosslink
Pitch
High capacity
Hard carbon
Sodium-ion batteries

ABSTRACT

As the precursor material inherently determines the fundamental structure of hard carbons, a direct manipulation of precursors at the molecular level promises enhanced flexibility in designing hard carbon architectures, which plays a pivotal role in dictating the final microstructural properties and, ultimately, the overall sodium storage performance. In this study, we present a novel generalized strategy utilizing P and O double cross-linking to convert pitch into a thermosetting precursor, creating copious micropores within pitch-based carbon. These micropores serve as essential pathways and active binding sites for sodium ion transport and storage, leading to pitch-derived hard carbons with a remarkable specific capacity of 416.1 mAh/g and an impressive initial Coulombic efficiency of 89.7%. Extensive study revealed a strong correlation between the increased plateau capacity and the closed pore volume, validating the micropore-driven sodium ion storage mechanism. Our findings underscores the groundbreaking significance of cross-linking in precursor modification, paving the way for the design and synthesis of high-performance hard carbon anodes for next-generation Na-ion batteries.

1. Introduction

Na-ion batteries (NIBs) have gained widespread attention due to their abundance and affordability, making them an attractive complement to Li-ion batteries in various applications [1-3]. The development of high-performing NIBs relies heavily on advancements in electrode materials, particularly on the anode side where options remain limited [4]. Of the available options, disordered carbons, particularly hard carbons, stand out as the most promising candidate for practical applications due to their ability to enhance the energy density of NIBs through their unique low-potential plateau capacity [5,6].

In the past decades, plenty of research has focused on designing carbon anodes by adopting various carbon precursors and controlling carbonization conditions, aiming to create more active sites for sodium storage [7,8]. Meanwhile, researchers have worked to uncover the fundamental mechanisms underlying sodium storage in these materials, examining factors such as interlayer distance [9,10], surface area [11,12], defect concentration [13], and pore structure [14,15] to better understand how they impact anode performance. Key findings from these studies are: (1) thermosetting precursors, including biomass [16,17], hydrocarbons [18,19], and resins [20,21], generally exhibit plateau capacity, whereas thermoplastic precursors like coke [22], tar [23], and pitch [24] tend to display sloping capacity. (2) carbonization temperatures play a crucial role in determining the final properties of carbon anodes, where higher temperatures are often employed to minimize defects [13], decrease interlayer distance [18] and surface area [25], as well as increase pore size [26,27]. (3) Additionally, there is growing recognition that closed pores may be beneficial for enhancing plateau capacity [28,29]. These gaining deeper insights help develop optimized strategies to design high-capacity carbon anodes for NIBs that outperform traditional graphite anodes in terms of Li storage.

Extensive research have demonstrated the feasibility of achieving

* Corresponding author.
E-mail address: yxlu@iphy.ac.cn (Y. Lu).

https://doi.org/10.1016/j.ensm.2024.103543
Received 26 March 2024; Received in revised form 14 May 2024; Accepted 8 June 2024
Available online 9 June 2024

sodium storage capacities in excess of 400 mAh/g using hard carbon anodes. Our previous research showed that tailoring pore structure through high-temperature treatment [14] and ethanol thermal synthesis [15] could significantly improve capacity, surpassing this benchmark. Further advancements were made by Komaba et al [30], who synthesized ultra-high capacity hard carbon using MgO templates with a maximum capacity of 484 mAh/g. Subsequent works by Yang [31] and Cao [32] utilized sieving and space-confined chemical vapor deposition (SC-CVD) techniques to control the porosity of the porous carbon to achieve reversible capacities of 482 mAh/g and 435.5 mAh/g, respectively. More recently, Wang et al. [33] used waste wood as a precursor to tune the crystallinity and amorphous content to achieve a reversible capacity of 430 mAh/g. While the importance of pore structure in boosting capacity has been well-established, the real hurdle is how to blend inexpensive raw materials with a simple yet effective method to craft affordable, high-performance hard carbon anodes, which is essential for their widespread practical use. Given our previous success in generating the plateau capacity of pitch-derived carbon through preoxidation in 2018 [34], our current focus is on refining this technique to unlock even higher levels of capacity from low-cost and high carbon yield pitch-based carbon sources. By doing so, we aim to bridge the gap between performance and affordability, accelerating the commercial viability of high-capacity carbon anodes in NIB applications.

In this study, we present a simple strategy for enhancing the plateau capacity of pitch-based hard carbon by integrating pre-oxidation and phosphoric acid treatment. The introduction of oxygen-containing functionalities during pre-oxidation creates favorable binding sites for phosphoric acid and promotes its subsequent cross-linking with the carbon framework. Moreover, additional exposure to preheat and wash steps introduces abundant micropores throughout the structure, fostering improved electrochemical activity. Upon carbonization, these tiny cavities coalesce into highly desirable "closed pores" to enable enhanced sodium uptake and release. These innovations culminate in a promising test outcome of 416.1 mAh/g reversible capacity and 89.7% initial Coulomb efficiency (ICE), suggesting considerable promise for future applications. Furthermore, this versatile methodology holds potential for extension to diverse types of carbon precursors and underscores the pivotal role played by well-designed pore structures in achieving high capacity carbon anodes.

2. Results and discussion

2.1. Preparation and characterization of pitch-derived samples

Pitch precursors are thoroughly mixed with phosphoric acid before undergoing pre-oxidation treatment in a furnace. To identify suitable incubation temperature, the thermogravimetry analysis (TGA) and differential scanning calorimetry (DSC) were performed to study the pyrolysis process of pitch and phosphoric acid mixtures (P&P) in both nitrogen and air atmospheres (Fig. S1). The weight of P&P in air initially decreases to about 170°C due to water evaporation and then increases dramatically attributed to air oxidation of the pitch. Furthermore, an exothermic peak in the DSC curve occurs at about 220°C, this process corresponds to the dehydration of oxygen-containing functional groups catalyzed by phosphoric acid and the subsequent formation of a stable P–O–C cross-linked structure [35,36]. In contrast, the TGA curve of P&P under nitrogen atmosphere experiences continuous weight loss between 170°C and 300°C with no discernible exothermic peak evident in the accompanying DSC curve, highlighting the importance of pre-oxidation treatment for forming intermolecular linkages between pitch and phosphoric acid. Hence, 220°C was selected as the pre-oxidation temperature for succeeding experiments. After preoxidation treatment, the P&P mixture was preheated at 600°C for 2 h under Ar atmosphere and washed with deionized water to neutral (denoted as POP_X-600, x is the weight percentage of phosphoric acid, such as 50, 60, 70, 80). Finally, the obtained sample was carbonized at high temperature for 3 h under Ar atmosphere to produce hard carbon anodes (denoted as POP_X-600-T, T is the high carbonization temperature, such 1400, 1500, 1600). To interpret how the presence or absence of O_2 and H_3PO_4 affects their properties during the following processes, besides the POP_{50}-600-1600, three controlled samples were synthesized, where the P&P mixture treated in N_2 is denoted as PNP_{50}-600-1600 while the pitch precursor directly treated in air or N_2 without mixing with H_3PO_4 are denoted as PO-600-1600 and PN-600-1600, respectively. The detailed synthesis process is shown in the Supporting Information.

The digital photos displayed in Fig. S2 show pitch precursors subjected to varying atmospheric conditions and combined with or without H_3PO_4 prior to (eg. PN, PO, PNP_{50}, POP_{50}) and after preheating at 600°C (eg. PN-600, PO-600, PNP_{50}-600, POP_{50}-600). The samples appear in powder form before the preheat treatment, with their colors gradually turning from brown to black. After preheating, however, samples treated in nitrogen transform into porous foam blocks, irrespective of the presence of H_3PO_4. This transformation arises from the pitch melting alongside the rapid escape of gases through thermal decomposition of the samples. In contrast, when exposed to air, the pitch can cross-link with oxygen molecules, altering the pyrolysis process from liquid to solid [34]. Note that due to the relatively low pre-oxidation temperature (<300°C), the cross-linking is insufficient for PO-600, causing it to remain in bulk form. Conversely, POP_{50}-600 is in the powder, indicating a higher degree of cross-linking resulting from the combination of oxygen and phosphoric acid.

The SEM images of the different hard carbon samples carbonized at 1600°C show that they have irregular particle shapes with sizes ranging from 5-20 μm (Fig. S3). However, PN-600-1600 and PNP_{50}-600-1600 have larger particle sizes of 15-20 μm due to particle aggregation caused by melting during the carbonization process. The microstructures of hard carbon samples can be visualized from high-resolution transmission electron microscopy (HRTEM) images (Fig. 1). PN-600-1600 and PNP_{50}-600-1600 have a high degree of order in their graphite microcrystalline structures, characterized by parallel accumulation of graphite flakes and a small interlayer spacing of 0.344 and 0.351 nm, respectively. In contrast, PO-600-1600 has a highly disordered turbostratic structure with randomly arranged bent graphene layers and an expanded interlayer spacing of 0.359 nm, indicating that pre-oxidation prevented graphitization. POP_{50}-600-1600 exhibits a honeycomb-like microstructures with large internal pores interconnected with graphitic layers, akin to our previous research findings [14]. Also, the interlayer spacing in POP_{50}-600-1600 is more expansive (0.361 nm) compared to PO-600-1600. All these features collectively contribute to more efficient transportation and improved storage capabilities for sodium-ion. As the phosphoric acid content increased, the turbostratic structure became more pronounced, with graphitic layers forming a large number of closed voids, as shown in Fig. S4, providing ample space for Na ion storage.

XRD and Raman spectroscopies were conducted to further investigate the microstructure of hard carbon samples. The XRD patterns in Fig. 2a show the sharp (002) peak for PN-600-1600, which is gradually broadened after H_3PO_4 or/and preoxidation treatment. PO-600-1600 has a broader peak compared to PNP-600-1600, indicating greater structural disorder within its crystal structure. On the other hand, POP_X-600-1600 treated with both preoxidation and phosphoric acid exhibits more disordered structure than those treated solely with preoxidation or H_3PO_4 alone, as evidenced by the smallest La and Lc shown in Fig. 2c. Increasing the phosphoric acid content from 50% to 80% led to slight changes in the graphite microcrystalline structure of the samples (Fig. S5 and Table S1), implying that the increase in phosphoric acid content doesn't substantially alter the graphitic structure of the samples. Raman spectroscopy was performed on samples to estimate the defect in the hard carbon materials. As show in Fig. 2b, all Raman spectra show two characteristic bands at around 1340 cm^{-1}(D band) and 1580 cm^{-1}(G band), which correspond to the degree of disorder and graphitization of the carbon material, respectively [37]. The peak intensity ratio (I_D/I_G)

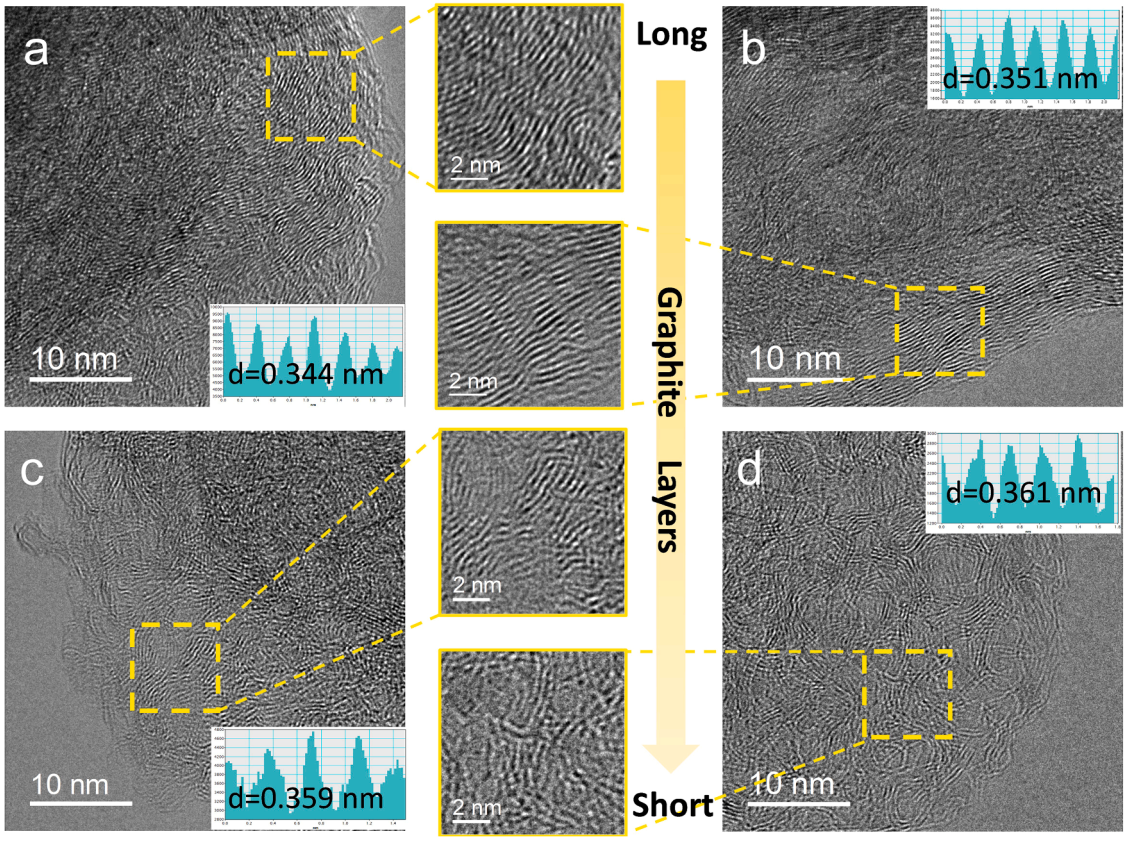

Fig. 1. HRTEM images of (a) PN-600-1600, (b) PNP_{50}-600-1600, (c) PO-600-1600 and (d) POP_{50}-600-1600. The inset shows the corresponding FFT patterns.

increases from 1.12 for PN-600-1600 to 1.56 for POP_{50}-600-1600 and further to 1.78 for POP_{80}-600-1600 (Fig. 2c and Fig. S6), suggesting a higher degree of structure disorder due to the inhibitory impact of the generated P–O–C cross-linkages on the graphitization process of pitch under the dual action of oxygen and phosphoric acid. The XRD and Raman results are consistent with HRTEM observations, further demonstrating that the co-treatment of pre-oxidation and phosphoric acid more effectively enhances the disorder of pitch-based hard carbon materials.

The N_2 and CO_2 adsorption-desorption test are employed to characterize the specific surface area and pore size distribution of carbon materials. According to Fig. 2d, the isotherms of PN-600 and PNP_{50}-600 can be classified as Type - II, which signifies a non-porous or macroporous material profile [38]. The isotherms of PO-600 and POP_{50}-600 represent type I, indicating the presence of micropores with diameters less than 2 nm [39]. The formation of porous structures is primarily due to the cross-linking process, which fundamentally transforms the carbonization pathway from a liquid to solid phase, thereby playing a pivotal role in creating and enhancing these fine-scale porous networks. The pore size distribution curve of POP_{50}-600 shows the majority of pores are within the 0.5 to 1.0 nm range (Fig. 2e). Changing N_2 to CO_2 for isothermal adsorption test allows for a more precise analysis of pore structures smaller than 1 nm. As shown in Fig. S7 and Fig. 2f, the POP_{50}-600 has the smallest pore size within the ranges of 0.3–0.4 nm when compared to other samples. Fig. 2g and Table S2 reveal the microporous volume constitutes over 95% of the total pore volume, thereby reinforcing the prevalence of microporosity in the sample. With the gradual increase of phosphoric acid addition, the micropores were significantly developed (see Fig. S8 and Table S2). It seems the addition of phosphoric acid plays a pivotal role in the formation of micropores, aligning with the established mechanism of the phosphoric acid activation process. The oxygen-containing functional groups such as OH formed during the pre-oxidation process of pitch can serve as active sites and crosslink with phosphoric acid to form a stable P–O–C structure. In the subsequent preheating process, they can mitigate the shrinkage of the carbon layer and decompose into polyphosphate, which can be removed by water washing, leaving pores in the carbon skeleton [40].

With further high-temperature carbonization at 1600°C, the isotherms of all samples can be classified as Type - II (Fig. 2h and Fig. S9), where the SSA and pore volume are significant reduced compared to the preheated carbon samples (Table S1). This indicates that high-temperature treatment can effectively shrink or close the pores within carbon materials, thereby reducing their SSA and pore volume, which is conducive to enhancing sodium storage capacity and improving the initial Coulombic efficiency. However, an excessive amount of phosphoric acid will lead to over-activation of the pitch precursor, stimulating the formation of mesopores while hindering the development of microporous, which is not beneficial for achieving favorable performance. Small-angle X-ray scattering (SAXS) analysis was used to further analyze the average pore size of the samples (Fig. 2i). A shoulder-shaped scattering at q around 0.1–0.3 $Å^{-1}$ originates from the micropores in the carbon bulk [41]. The PN-600-1600 and PNP_{50}-600-1600 samples do not exhibit any distinct humps, suggesting they have a scarcity or absence of significant microporosity. Conversely, PO-600-1600 and POP_{50}-600-1600 samples display broad humps within the range, indicating they possess an abundance of micropores. Increasing phosphoric acid amount is linked with a slight boost in hump intensity, indicative of increased porosity in the samples (Fig. S10). Based on SAXS data, the SSA^{SAXS} and average pore diameter (R) calculated by Teubner-Strey model are shown in the Table S3. It can be seen that all POP_X-600 samples carbonized at the same temperature of 1600°C with varying phosphoric acid amount, consistently display high SSA^{SAXS} values exceeding 900 $m^2\ g^{-1,}$ and R gradually decreases from 2.5 nm to 1.9 nm as the amount of phosphoric acid increases. It could be inferred that

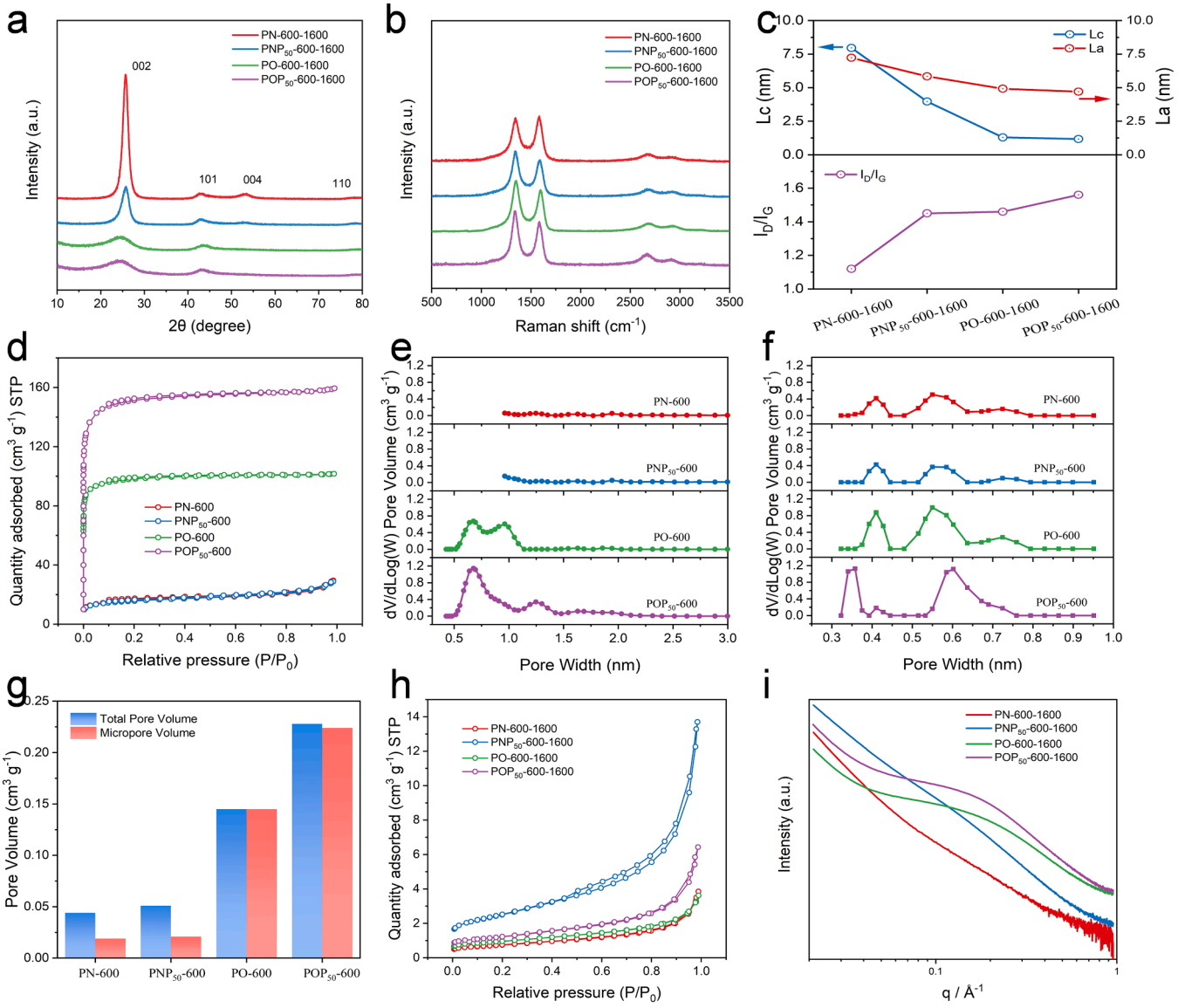

Fig. 2. (a) XRD patterns, (b) Raman spectra, (c) Summary of Lc, La, and I_D/I_G structural parameters, (d) The N_2 adsorption-desorption isotherms of preheated carbon, (e) The pore size distribution (N_2), (f) The pore size distribution (CO_2), (g) Total pore volume and micropore volume of preheated carbon, (h) The N_2 adsorption-desorption isotherms of hard carbon, (i) SAXS patterns.

open pores tend to undergo a process of closure and coalescence at high temperature treatment, ultimately forming larger internal pores, aligning with findings reported in the literature [42]. The increased SSA^{SAXS} and suitable pore diameter can enhance the adsorption and release of sodium ions, which is the key to obtain high plateau capacity [31].

2.2. Sodium storage behaviors of pitch-derived carbon anodes

Galvanostatic charge and discharge (GCD) test are conducted between 0–2.0 V (vs. Na^+/Na) at a current density of 20 mA/g. The first cycles of GCD curves of hard carbon are shown in Fig. 3a. The PN-600-1600 and PNP_{50}-600-1600 electrodes only present slope voltage curves with capacities of 67.8 mAh/g and 98.5 mAh/g as well as low ICE of 55.4% and 62%, respectively. The low capacity and ICE are attributed to the high graphitization degree and small d_{002} of the samples, which are not conducive to sodiation/desodiation. However, the PO-600-1600 and POP_x-600-1600 electrodes both display a typical GCD curve of hard carbon materials with a high-potential sloping region (1–0.1 V) and a low-potential plateau region (0.1–0 V). The samples POP_{50}-600-1600, POP_{60}-600-1600, POP_{70}-600-1600, and POP_{80}-600-1600 display remarkable reversible capacities of 359.3, 387.7, 416.1 and 403.5 mAh/g, respectively, with high ICE of 89.8, 90.6, 89.7 and 87.0% respectively. Meanwhile, there's an obvious increase in the plateau capacity contribution, escalating from 310.2 mAh/g for POP_{50}-600-1600 to a peak of 371.7 mAh/g for POP_{70}-600-1600 (Fig. 3b). Most notably, the cross-linked pitch subjected to both pre-oxidation and phosphoric acid treatment has shown unprecedented reversible capacity and ICE among all known pitch-derived carbon anodes for Na storage (Fig. 3c and Table S4), underscoring the significant success of the innovative phosphate-oxygen double cross-linking strategy.

To evaluate the practical application of P/O dual crosslinked pitch-derived carbon anodes, full cells with the $Na[Ni_{0.4}Fe_{0.2}Mn_{0.4}]O_2$ cathode (NFM424) and the POP_{70}-600-1600 anode were fabricated and measured (Fig. 3d–e). The full cells deliver a reversible capacity of 155 mAh/g (based on the cathode), an average operating voltage of 3.3 V and a high ICE of 84.35% at a current density of 17 mA/g. The energy density of full battery was calculated to be 364 Wh/kg, based on the total mass of the cathode and anode. While the hard carbon anode exhibits underwhelming rate performance and cycling stability in half-cell tests, as depicted in Fig. S11, largely due to the substantial overpotential

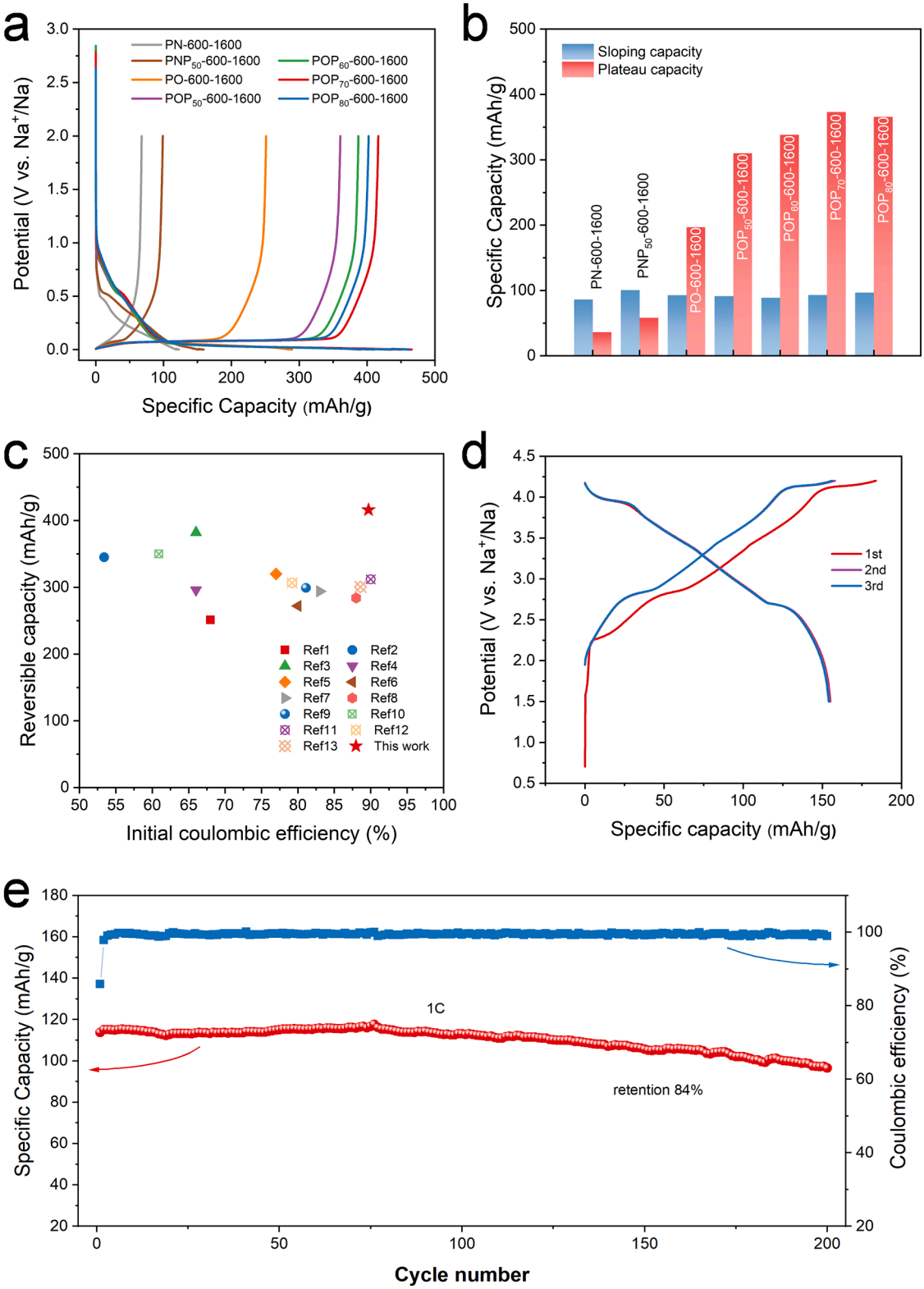

Fig. 3. (a) Initial charge and discharge curves for hard carbon, (b) Sloping capacity and plateau capacity of hard carbon, (c) Comparison of the capacity and ICE of POP_{70}-600-1600 anode with that of pitch-based anodes recently reported in NIBs, (d) Initial charge and discharge curves and (e) Cycle performance of NFM424//POP_{70}-600-1600 full cell.

of the sodium metal electrode when used with an ester electrolyte [43], the full cell configuration still manages to deliver a commendable specific capacity of 113 mAh/g even at 1C. Moreover, it demonstrates excellent cycling durability, retaining 84% of its original capacity after 200 cycles. To further reduce cost and increase energy density, we can use aluminum foil instead of copper foil and employ eco-friendly CMC/SBR binder in this system.

As evidenced by the obtained electrochemical measurements, it is clear that although the microcrystalline structures of these POP_X-600-1600 samples show minimal variation based on the previous HRTEM

and XRD data, there is a notable increase in their plateau capacity (Fig. 3b), indicating that the sodium storage mechanism in the plateau region is not related to an intercalation mechanism. Fig. S12 and Table S5 demonstrate that higher carbonization temperature enhances ICE and plateau capacity of hard carbon while decreasing slope capacity. This implies that high temperatures effectively eliminate defects and heteroatoms, reducing irreversible capacity, and promote the formation of closed pores. This structural transformation dramatically boosts the volume of closed pores, enhancing the accommodation of sodium ions within these confined spaces, thereby correlating with the enhanced plateau capacity observed. Our previous research established a connection between the plateau capacity of carbon materials and their closed pore structures [14,15,44,45] via the skeletal density analysis using helium (He) probe. Nonetheless, no discernible linear correlation was yielded between the plateau capacity of POP_X-600-1600 samples and the He-derived closed pore volume (Fig. S14a). This discrepancy prompts us to expand the scope of "closed" pores, which is defined as inaccessible to electrolyte molecules but permeable to sodium ions. We propose distinguishing between fully closed pores (FCP), which are inaccessible to He, and semiclosed pores (SCP), which can be accessed by He but not electrolytes, yet still serve as active sodium storage sites. To account for the total volume of combined closed pores (CCP, which is FCP+SCP) (Fig. 4a), we employed the specific gravity method using dimethyl carbonate (DMC) as the immersion medium to measure the CCP volume of hard carbon samples (details in Supporting Information Note S3 and Note S4). As depicted in Fig. 4b, there's a strong positive correlation between CCP and the plateau capacity, which suggests that the combined closed pores-those impermeable to electrolytes – are the primary sites for sodium ion storage to generate the plateau capacity.

2.3. *Exploring crosslinking mechanisms & evaluating strategy effectiveness*

Fourier Transform Infrared spectroscopy (FTIR) was employed to identify and analyse the various functional groups present in the treated pitch samples prior to preheat treatment. As shown in Fig. 5a all samples demonstrate aromatic C═C stretching at 1600 cm^{-1} and aromatic C–H out-of-plane deformation bands at 740–870 cm^{-1} [46,47]. Notably, the FTIR spectra of PO samples exhibit distinct absorption bands that indicate the presence of O—H groups, where stretching vibrations occurring in the range of 3300–3600 cm^{-1} and 3300–3100 cm^{-1} correspond to aromatic phenols and carboxylic acid association, respectively [48]. The appearance of C═O stretching vibrations at 1770 cm^{-1} and 1700 cm^{-1} confirms the presence of carboxylic functional groups, indicating pre-oxidation reactions taken place during the air exposure stage [49,50]. Despite these oxidative modifications, PO samples still retain several characteristic vibrational modes akin to the PN and PNP_{50} samples. For instance, the aromatic C—H stretching vibration at 3000–3100 cm^{-1}, aliphatic C—H stretching vibration at 2800–3000 cm^{-1} as well as aliphatic C—H deformation vibration at 1300–1490 cm^{-1} [47]. However, absorption peaks of C—H and O—H groups presented in PO samples become weak or even disappear in POP_{50} samples, indicating that phosphoric acid crosslinks with oxygen-containing functional groups on pitch materials to accelerated dehydration and pyrolysis. The denoted rectangular region within 1300–1000 cm^{-1} can be attributed to the overlapping absorption bands of various oxygen and phosphorus functional groups including P═O, C—O and P—O—C linkages [51,52].

X-ray photoelectron spectroscopy (XPS) was employed to further understand the element composition and valence state. Before testing, all samples underwent rigorous washing with deionized water until reaching a neutral pH level to mitigate any influence from residual free phosphoric acid. The peaks at 284.6 eV and 533.2 eV in the survey spectra (Fig. 5b) are assigned as C 1s and O 1s respectively. The high-resolution C 1s spectra for each sample are shown in Fig. 5c–f. Six peaks center at 284.3, 284.8, 285.8, 286.9, 288.7, and 290.4 eV correspond to graphitic C═C, aliphatic C—C, C—O, C═O, O—C═O, and π-π* bonds, respectively [53,54]. Both PO and POP_{50} samples contain a higher proportion of C—O and O═C—O functional groups compared to PN and PNP_{50}, which is consistent with the FTIR results. To be noticed, POP_{50} possesses a high content of π - π* bonds, which can be attributed to two main factors: (1) the reduced presence of alkyl side chains (Table 1) encourages stronger π-π interactions among the polynuclear aromatic components within the pitch matrix [55,56]; (2) the incorporation of phosphate groups, known for their strong electron affinity, contributes to enhancing π-π interactions between pitch molecules when they attach to the side chains of aromatic nuclei [57].

The P 2p fitted spectra of POP_{50} samples with different preheat temperatures are shown in Fig. S15. It becomes evident that when the heat treatment surpasses 450°C a new feature of C_2–P–O_2 group emerges besides the C–P–O_3, C–O–P and PO_4 groups, implying more carbon atoms tend to bind to the same phosphorus atom. The formation of P-bridging through C_2–P–O_2 configurations can effectively links and crosslinks the aromatic segments, thereby creating a more stable three-dimensional network structure [58], which facilitates the formation of hard carbons with higher disorder degree. The XPS spectrum of the hard carbon sample after high-temperature treatment at 1600°C is shown in Fig. S16, which contains a small amount of phosphorus (less than 0.2%). This is because the water washing step after pre-heating removes most of the phosphorus element. In addition, upon exposure to high temperatures, P and O heteroatoms are effectively removed, resulting in pitch-derived hard carbon with minimal heteroatom content, which

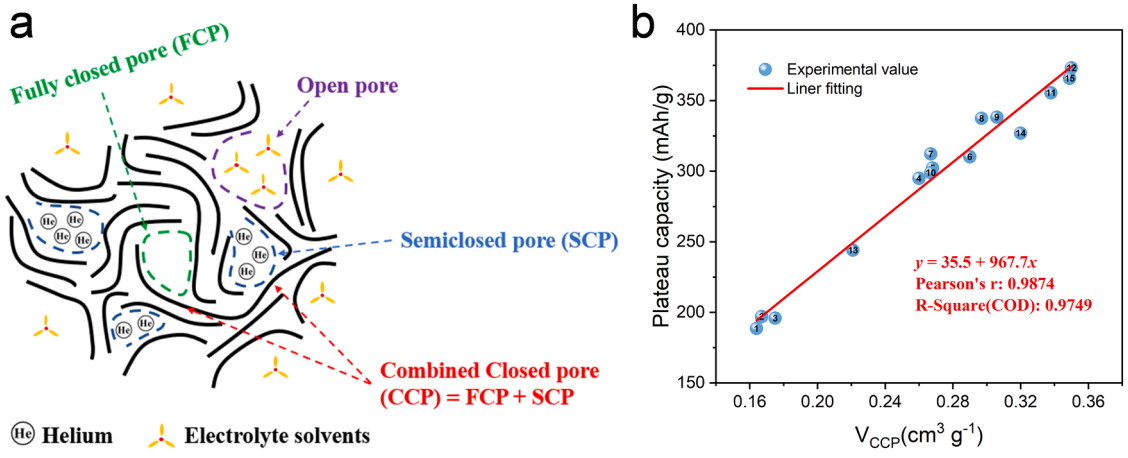

Fig. 4. (a) Schematic diagram of the closed pores in hard carbon. (b) Linear plot between the V_{CCP} and the plateau capacity. CCP: inaccessible to electrolytes; SCP: accessible to helium but inaccessible to electrolytes; FCP: inaccessible to both helium and electrolytes.

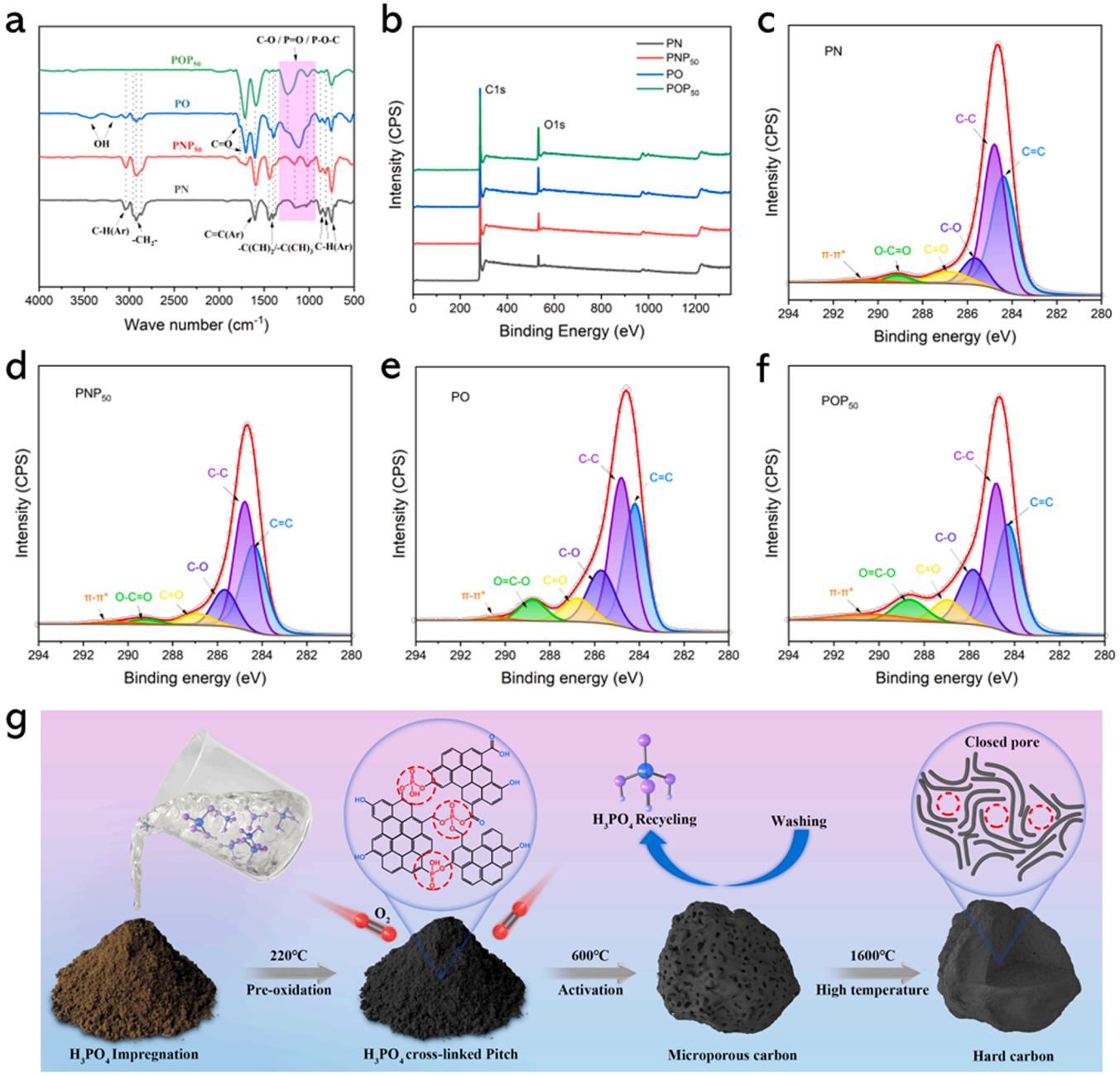

Fig. 5. (a) The FTIR spectroscopy spectra of PN, PNP_{50}, PO and POP_{50}, (b) overall XPS spectra of PN, PNP_{50}, PO and POP_{50}, High-resolution C1s XPS spectra of (c) PN, (d) PNP_{50}, (e) PO and (f) POP_{50}, (g) Schematic illustration of pitch-based hard carbon synthesis.

Table 1
The content of the C 1s peaks for each sample by Gaussian distribution fitting.

Samples	C═C & C—C (%)	C—O (%)	C═O (%)	O═C—O (%)	π-π* (%)
PN	82.14	8.19	5.66	2.44	1.57
PNP_{50}	81.35	8.74	5.62	2.47	1.71
PO	68.95	15.95	7.82	6.20	1.07
POP_{50}	65.31	15.81	6.87	7.35	4.66

contributes to an enhanced Coulombic efficiency.

Therefore, the collective evidence supports the notion that the pitch materials first undergo oxidation to generate a substantial quantity of oxygen-containing functional groups (mainly OH and COOH), which then interact with phosphoric acid to form a stable cross-linked structure, as shown in Fig. 5g. This structure breaks down into soluble polyphosphoric acid during subsequent preheat treatment, which can be easily removed by water washing, creating a large number of nanopores within the carbon skeleton. Subsequent high-temperature carbonization makes open pores to close and adjusts the size and number of closed pores. These refined nanopores provide a wealth of active sites suitable for sodium ion storage, thereby enhancing the material's capability for battery applications.

To validate the generality of the cross-linking strategy to boost the plateau capacity of hard carbon materials, two common precursors of bituminous coal and hazelnut shells were adopted. Given both precursors already contain a certain amount of oxygen-containing functional groups (Fig. S17), we directly treated them with phosphoric acid to promote the cross-linking reaction. As shown in Fig. S18, The reversible capacity of bituminous coal increased from 271.4 mAh/g (ICE

86.1%) to 406.2 mAh/g (ICE 89.3%) and the plateau capacity increased from 214.6 to 362.4 mAh/g by the cross-linking activation of phosphoric acid. As well, the hazelnut shell sample HSP_{30}-600-1400 has a high reversible capacity of 404.9 mAh/g (ICE 87.8%) and a plateau capacity of 343.6 mAh/g. These results highlight the versatile use of the method for producing high-capacity hard carbon and underscore the importance of oxygen-containing functional groups in phosphoric acid cross-linking.

3. Conclusion

In summary, a pitch based hard carbon with both high reversible capacity (416.1 mAh/g) and high initial Coulombic efficiency (89.7%) was synthesized through a P and O double crosslinking strategy. The stable cross-linking structure not only hinders the melting and ordered recombination of pitch, but also can generate a large number of uniform micropores (~2 nm) in the carbon matrix during the subsequent activation process. Following high-temperature treatment, these micropores undergo transformation into semiclosed pores (accessible to He but not electrolytes) and fully closed pores (inaccessible to He), thereby acting as active sites for sodium ion storage. This results in the achievement of ultra-high plateau capacity (371.7 mAh/g). Furthermore, the experimental results unveiled a strong positive correlation between the plateau capacity and the volume of closed pores, which facilitates sodium ion storage. Importantly, this innovative cross-linking strategy is also applicable to a variety of precursor materials such as coal-based and biomass sources, thereby establishing itself as a broadly adaptable method for manufacturing high-capacity hard carbon anodes. Our research highlights the paramount importance of cross-linking in manipulating precursor structures, charting a new course for designing advanced high-performance hard carbon anodes in NIBs.

CRediT authorship contribution statement

Xiaobing Zhao: Writing – original draft, Investigation, Conceptualization. **Peng Shi:** Formal analysis. **Haibo Wang:** Validation. **Qingshi Meng:** Resources. **Xingguo Qi:** Resources. **Guanjie Ai:** Validation. **Fei Xie:** Resources, Funding acquisition. **Xiaohui Rong:** Resources. **Ying Xiong:** Resources. **Yaxiang Lu:** Writing – review & editing, Supervision, Funding acquisition. **Yong-Sheng Hu:** Writing – review & editing, Resources.

Declaration of competing interest

The authors declare that they have no known competing financial interests or personal relationships that could have appeared to influence the work reported in this paper.

Data availability

I have shared the link to my data/code at the attach file step

Acknowledgements

This work was supported by the National Key R&D Program of China (2022YFB3807800), National Natural Science Foundation (NSFC) of China (52122214, 52072403, 22339001), and Youth Innovation Promotion Association of the Chinese Academy of Sciences (2020006).

Supplementary materials

Supplementary material associated with this article can be found, in the online version, at doi:10.1016/j.ensm.2024.103543.

References

[1] P.K. Nayak, L. Yang, W. Brehm, P. Adelhelm, From lithium-ion to sodium-ion batteries: advantages, challenges, and surprises, Angew. Chem. Int. Ed. 57 (2017) 102–120, https://doi.org/10.1002/anie.201703772.
[2] E. Goikolea, V. Palomares, S. Wang, I.R. de Larramendi, X. Guo, G. Wang, T. Rojo, Na-Ion batteries—approaching old and new challenges, Adv. Energy Mater. 10 (2020) 2002055, https://doi.org/10.1002/aenm.202002055.
[3] R. Dang, Y. Lu, X. Rong, F. Ding, Q. Guo, W. Xu, L. Chen, Y.-S. Hu, Research progress of key materials and engineering exploration for Na-ion batteries, Chin. Sci. Bull. 67 (2022) 3546–3564, https://doi.org/10.1360/tb-2022-0245.
[4] Y. Chu, J. Zhang, Y. Zhang, Q. Li, Y. Jia, X. Dong, J. Xiao, Y. Tao, Q.H. Yang, Reconfiguring hard carbons with emerging sodium-ion batteries: a perspective, Adv. Mater. 35 (2023) e2212186, https://doi.org/10.1002/adma.202212186.
[5] F. Xie, Z. Xu, Z. Guo, M.-M. Titirici, Hard carbons for sodium-ion batteries and beyond, Prog. Energy 2 (2020) 042002, https://doi.org/10.1088/2516-1083/aba5f5.
[6] D. Chen, W. Zhang, K. Luo, Y. Song, Y. Zhong, Y. Liu, G. Wang, B. Zhong, Z. Wu, X. Guo, Hard carbon for sodium storage: mechanism and optimization strategies toward commercialization, Energy Environ. Sci. 14 (2021) 2244–2262, https://doi.org/10.1039/d0ee03916k.
[7] Z. Zeng, Y. Mao, Z. Hu, K. Chen, Q. Huang, Y. Song, Z. Wu, P. Zhang, T. Chen, X. Guo, Research progress and commercialization of biologically derived hard carbon anode materials for sodium-ion batteries, Ind. Eng. Chem. Res. 62 (2023) 15343–15359, https://doi.org/10.1021/acs.iecr.3c00818.
[8] E. Irisarri, N. Amini, S. Tennison, C.M. Ghimbeu, J. Gorka, C. Vix-Guterl, A. Ponrouch, M.R. Palacin, Optimization of large scale produced hard carbon performance in Na-Ion batteries: effect of precursor, temperature and processing conditions, J. Electrochem. Soc. 165 (2018) A4058–A4066, https://doi.org/10.1149/2.1171816jes.
[9] S. Qiu, L. Xiao, M.L. Sushko, K.S. Han, Y. Shao, M. Yan, X. Liang, L. Mai, J. Feng, Y. Cao, X. Ai, H. Yang, J. Liu, Manipulating adsorption–insertion mechanisms in nanostructured carbon materials for high-efficiency sodium ion storage, Adv. Energy Mater. 7 (2017) 1700403, https://doi.org/10.1002/aenm.201700403.
[10] N. Sun, Z. Guan, Y. Liu, Y. Cao, Q. Zhu, H. Liu, Z. Wang, P. Zhang, B. Xu, Extended "Adsorption–Insertion" model: a new insight into the sodium storage mechanism of hard carbons, Adv. Energy Mater. 9 (2019) 1901351, https://doi.org/10.1002/aenm.201901351.
[11] Q. Li, Y. Zhu, P. Zhao, C. Yuan, M. Chen, C. Wang, Commercial activated carbon as a novel precursor of the amorphous carbon for high-performance sodium-ion batteries anode, Carbon 129 (2018) 85–94, https://doi.org/10.1016/j.carbon.2017.12.008.
[12] H. Lu, X. Chen, Y. Jia, H. Chen, Y. Wang, X. Ai, H. Yang, Y. Cao, Engineering Al2O3 atomic layer deposition: enhanced hard carbon-electrolyte interface towards practical sodium ion batteries, Nano Energy 64 (2019) 103903, https://doi.org/10.1016/j.nanoen.2019.103903.
[13] L. Xiao, H. Lu, Y. Fang, M.L. Sushko, Y. Cao, X. Ai, H. Yang, J. Liu, Low-defect and low-porosity hard carbon with high coulombic efficiency and high capacity for practical sodium ion battery anode, Adv. Energy Mater. 8 (2018) 1703238, https://doi.org/10.1002/aenm.201703238.
[14] C. Zhao, Q. Wang, Y. Lu, B. Li, L. Chen, Y.-S. Hu, High-temperature treatment induced carbon anode with ultrahigh Na storage capacity at low-voltage plateau, Sci. Bull. 63 (2018) 1125–1129, https://doi.org/10.1016/j.scib.2018.07.018.
[15] Q. Meng, Y. Lu, F. Ding, Q. Zhang, L. Chen, Y.-S. Hu, Tuning the closed pore structure of hard carbons with the highest Na storage capacity, ACS Energy Lett. 4 (2019) 2608–2612, https://doi.org/10.1021/acsenergylett.9b01900.
[16] C. del Mar Saavedra Rios, L. Simonin, C.M. Ghimbeu, C. Vaulot, D. da Silva Perez, C. Dupont, Impact of the biomass precursor composition in the hard carbon properties and performance for application in a Na-ion battery, Fuel Process. Technol. 231 (2022) 107223, https://doi.org/10.1016/j.fuproc.2022.107223.
[17] J. Wang, J. Zhao, X. He, Y. Qiao, L. Li, S.-L. Chou, Hard carbon derived from hazelnut shell with facile HCl treatment as high-initial-coulombic-efficiency anode for sodium ion batteries, Sustain. Mater. Technol. 33 (2022) e00446, https://doi.org/10.1016/j.susmat.2022.e00446.
[18] K. Kubota, S. Shimadzu, N. Yabuuchi, S. Tominaka, S. Shiraishi, M. Abreu-Sepulveda, A. Manivannan, K. Gotoh, M. Fukunishi, M. Dahbi, S. Komaba, Structural analysis of sucrose-derived hard carbon and correlation with the electrochemical properties for lithium, sodium, and potassium insertion, Chem. Mater. 32 (2020) 2961–2977, https://doi.org/10.1021/acs.chemmater.9b05235.
[19] Z. Xu, J. Wang, Z. Guo, F. Xie, H. Liu, H. Yadegari, M. Tebyetekerwa, M.P. Ryan, Y. S. Hu, M.M. Titirici, The role of hydrothermal carbonization in sustainable sodium-ion battery anodes, Adv. Energy Mater. 12 (2022) 202200208, https://doi.org/10.1002/aenm.202200208.
[20] G. Hasegawa, K. Kanamori, N. Kannari, J.i. Ozaki, K. Nakanishi, T. Abe, Hard carbon anodes for Na-Ion batteries: toward a practical use, ChemElectroChem 2 (2015) 1917–1920, https://doi.org/10.1002/celc.201500412.
[21] X. Yin, Z. Lu, J. Wang, X. Feng, S. Roy, X. Liu, Y. Yang, Y. Zhao, J. Zhang, Enabling fast Na+ transfer kinetics in the whole-voltage-region of hard-carbon anodes for ultrahigh-rate sodium storage, Adv. Mater. 34 (2022) e2109282, https://doi.org/10.1002/adma.202109282.
[22] D. Zhao, H. Zhao, J. Ye, W. Song, S. Miao, H. Shen, Y. Zhao, M. Kang, Z. Li, Oxygen functionalization boosted sodium adsorption-intercalation in coal based needle coke, Electrochim. Acta 329 (2020) 135127, https://doi.org/10.1016/j.electacta.2019.135127.
[23] Y. Wang, N. Xiao, Z. Wang, H. Li, M. Yu, Y. Tang, M. Hao, C. Liu, Y. Zhou, J. Qiu, Rational design of high-performance sodium-ion battery anode by molecular

engineering of coal tar pitch, Chem. Eng. J. 342 (2018) 52–60, https://doi.org/10.1016/j.cej.2018.01.098.
[24] M. Jiang, N. Sun, R.Ali Soomro, B. Xu, The recent progress of pitch-based carbon anodes in sodium-ion batteries, J. Energy Chem. 55 (2021) 34–47, https://doi.org/10.1016/j.jechem.2020.07.002.
[25] H. Alptekin, H. Au, A.C.S. Jensen, E. Olsson, M. Goktas, T.F. Headen, P. Adelhelm, Q. Cai, A.J. Drew, M.-M. Titirici, Sodium storage mechanism investigations through structural changes in hard carbons, ACS Appl. Energy Mater. 3 (2020) 9918–9927, https://doi.org/10.1021/acsaem.0c01614.
[26] H. Au, H. Alptekin, A.C.S. Jensen, E. Olsson, C.A. O'Keefe, T. Smith, M. Crespo-Ribadeneyra, T.F. Headen, C.P. Grey, Q. Cai, A.J. Drew, M.-M. Titirici, A revised mechanistic model for sodium insertion in hard carbons, Energy Environ. Sci. 13 (2020) 3469–3479, https://doi.org/10.1039/d0ee01363c.
[27] V. Surendran, R.K. Hema, M.S.O. Hassan, V. Vijayan, M.M. Shaijumon, Open or Closed? Elucidating the correlation between micropore nature and sodium storage mechanisms in hard carbon, Batteries Supercaps 5 (2022) 202200316, https://doi.org/10.1002/batt.202200316.
[28] H. Kim, J.C. Hyun, D.H. Kim, J.H. Kwak, J.B. Lee, J.H. Moon, J. Choi, H.D. Lim, S. J. Yang, H.M. Jin, D.J. Ahn, K. Kang, H.J. Jin, H.K. Lim, Y.S. Yun, Revisiting lithium- and sodium-ion storage in hard carbon anodes, Adv. Mater. 35 (2023) e2209128, https://doi.org/10.1002/adma.202209128.
[29] X.X. He, W.H. Lai, Y. Liang, J.H. Zhao, Z. Yang, J. Peng, X.H. Liu, Y.X. Wang, Y. Qiao, L. Li, X. Wu, S.L. Chou, Achieving All-plateau and high-capacity sodium insertion in topological graphitized carbon, Adv. Mater. 35 (2023) e2302613, https://doi.org/10.1002/adma.202302613.
[30] A. Kamiyama, K. Kubota, D. Igarashi, Y. Youn, Y. Tateyama, H. Ando, K. Gotoh, S. Komaba, MgO-template synthesis of extremely high capacity hard carbon for Na-Ion battery, Angew. Chem. Int. Ed. 60 (2021) 5114–5120, https://doi.org/10.1002/anie.202013951.
[31] Q. Li, X. Liu, Y. Tao, J. Huang, J. Zhang, C. Yang, Y. Zhang, S. Zhang, Y. Jia, Q. Lin, Y. Xiang, J. Cheng, W. Lv, F. Kang, Y. Yang, Q.-H. Yang, Sieving carbons promise practical anodes with extensible low-potential plateaus for sodium batteries, Natl. Sci. Rev. 9 (2022) nwac084, https://doi.org/10.1093/nsr/nwac084.
[32] X. Chen, N. Sawut, K. Chen, H. Li, J. Zhang, Z. Wang, M. Yang, G. Tang, X. Ai, H. Yang, Y. Fang, Y. Cao, Filling carbon: a microstructure-engineered hard carbon for efficient alkali metal ion storage, Energy Environ. Sci. 16 (2023) 4041–4053, https://doi.org/10.1039/d3ee01154b.
[33] Z. Tang, R. Zhang, H. Wang, S. Zhou, Z. Pan, Y. Huang, D. Sun, Y. Tang, X. Ji, K. Amine, M. Shao, Revealing the closed pore formation of waste wood-derived hard carbon for advanced sodium-ion battery, Nat. Commun. 14 (2023) 6024, https://doi.org/10.1038/s41467-023-39637-5.
[34] Y. Lu, C. Zhao, X. Qi, Y. Qi, H. Li, X. Huang, L. Chen, Y.S. Hu, Pre-oxidation-tuned microstructures of carbon anodes derived from pitch for enhancing Na storage performance, Adv. Energy Mater. 8 (2018) 201800108, https://doi.org/10.1002/aenm.201800108.
[35] M. Jagtoyen, F. Derbyshire, Activated carbons from yellow poplar and white oak by H3PO4 activation, Carbon 36 (1998) 1085–1097, https://doi.org/10.1016/s0008-6223(98)00082-7.
[36] S. Yorgun, D. Yıldız, Preparation and characterization of activated carbons from Paulownia wood by chemical activation with H3PO4, J. Taiwan Inst. Chem. Eng. 53 (2015) 122–131, https://doi.org/10.1016/j.jtice.2015.02.032.
[37] A.C. Ferrari, J. Robertson, Interpretation of Raman spectra of disordered and amorphous carbon, Phys. Rev. B 61 (2000) 14095–14107, https://doi.org/10.1103/PhysRevB.61.14095.
[38] J.E.S.S. Lowell, Powder Surface Area and Porosity, Springer-Science+Business Media, B.V., Chapman and Hall, New York, 1991.
[39] J.C. Groen, L.A.A. Peffer, J. Pérez-Ramírez, Pore size determination in modified micro- and mesoporous materials. Pitfalls and limitations in gas adsorption data analysis, Microporous Mesoporous Mater. 60 (2003) 1–17, https://doi.org/10.1016/s1387-1811(03)00339-1.
[40] Z. Songlin, Review on phosphoric acid activation for preparation of activated carbon (I): roles of phosphoric acid, Chem. Ind. Forest Prod. 37 (2017) 1–9, https://doi.org/10.3969/j.issn.0253-2417.2017.03.001.
[41] D. Saurel, J. Segalini, M. Jauregui, A. Pendashteh, B. Daffos, P. Simon, M. Casas-Cabanas, A SAXS outlook on disordered carbonaceous materials for electrochemical energy storage, Energy Storage Mater. 21 (2019) 162–173, https://doi.org/10.1016/j.ensm.2019.05.007.
[42] A. Kamiyama, K. Kubota, T. Nakano, S. Fujimura, S. Shiraishi, H. Tsukada, S. Komaba, High-capacity hard carbon synthesized from macroporous phenolic resin for sodium-ion and potassium-ion battery, ACS Appl. Energy Mater. 3 (2019) 135–140, https://doi.org/10.1021/acsaem.9b01972.
[43] L. Yan, G. Zhang, J. Wang, Q. Ren, L. Fan, B. Liu, Y. Wang, W. Lei, D. Ruan, Q. Zhang, Z. Shi, Revisiting electrolyte kinetics differences in sodium ion battery: are esters really inferior to ethers? Energy Environ. Mater. 6 (2022) eem2.12523, https://doi.org/10.1002/eem2.12523.
[44] Y. Li, A. Vasileiadis, Q. Zhou, Y. Lu, Q. Meng, Y. Li, P. Ombrini, J. Zhao, Z. Chen, Y. Niu, X. Qi, F. Xie, R. van der Jagt, S. Ganapathy, M.-M. Titirici, H. Li, L. Chen, M. Wagemaker, Y.-S. Hu, Origin of fast charging in hard carbon anodes, Nat. Energy 9 (2024) 134–142, https://doi.org/10.1038/s41560-023-01414-5.
[45] Y. Li, Y. Lu, Q. Meng, A.C.S. Jensen, Q. Zhang, Q. Zhang, Y. Tong, Y. Qi, L. Gu, M. M. Titirici, Y.S. Hu, Regulating pore structure of hierarchical porous waste cork-derived hard carbon anode for enhanced Na storage performance, Adv. Energy Mater. 9 (2019) 1902852, https://doi.org/10.1002/aenm.201902852.
[46] Y.-L. Wang, X.-h. Chen, M.-j. Ding, J.-Z. Li, Oxidation of coal pitch by H2O2 under mild conditions, Energy Fuels 32 (2018) 796–800, https://doi.org/10.1021/acs.energyfuels.7b02010.
[47] P.N. Kuznetsov, E.S. Kamenskiy, L.I. Kuznetsova, Comparative study of the properties of the coal extractive and commercial pitches, Energy Fuels 31 (2017) 5402–5410, https://doi.org/10.1021/acs.energyfuels.7b00158.
[48] E. Genceli, E. Apak, M. Razvigorova, N. Petrov, V. Minkova, E. Ekinci, Preparation, modification, and characterization of pitches from apricot stones, Fuel Process. Technol. 75 (2002) 97–107, https://doi.org/10.1016/S0378-3820(01)00259-4.
[49] T. Guan, G. Zhang, J. Zhao, J. Wang, K. Li, Insight into the oxidative reactivity of pitch fractions for predicting and optimizing the oxidation stabilization of pitch, Fuel 242 (2019) 184–194, https://doi.org/10.1016/j.fuel.2019.01.034.
[50] K.H. Choi, S.-Y. Lee, I. Hong, S. Son, J.-C. An, S. Kim, Molecular-level investigation of coal-tar pitch treated by air blowing: Revealing the restructure of aromatic compounds via radical reactions, Carbon 203 (2023) 377–385, https://doi.org/10.1016/j.carbon.2022.11.022.
[51] A.M. Puziy, O.I. Poddubnaya, A. Martınez-Alonso, F. Suarez-Garcıa, J.M.D. Tascon, Synthetic carbons activated with phosphoric acid I. Surface chemistry and ion binding properties, Carbon 40 (2002) 1493–1505, https://doi.org/10.1016/S0008-6223(01)00317-7.
[52] Y. Zhang, H. Tao, J. Li, X. Yang, Achieving a high-performance P/C anode through P–O–C bond for sodium ion batteries, Ionics 26 (2020) 3377–3385, https://doi.org/10.1007/s11581-020-03486-9.
[53] R. Arrigo, M. Hävecker, S. Wrabetz, R. Blume, M. Lerch, J. McGregor, E.P. J. Parrott, J.A. Zeitler, L.F. Gladden, A. Knop-Gericke, R. Schlögl, D.S. Su, Tuning the acid/base properties of nanocarbons by functionalization via amination, J. Am. Chem. Soc. 132 (2010) 9616–9630, https://doi.org/10.1021/ja910169v.
[54] T.H. Lim, S.Y. Yeo, Investigation of the degradation of pitch-based carbon fibers properties upon insufficient or excess thermal treatment, Sci. Rep. 7 (2017) 4733, https://doi.org/10.1038/s41598-017-05192-5.
[55] H. Santos Silva, A. Alfarra, G. Vallverdu, D. Bégué, B. Bouyssiere, I. Baraille, Sensitivity of Asphaltene aggregation toward the molecular architecture under desalting thermodynamic conditions, Energy Fuels 32 (2017) 2681–2692, https://doi.org/10.1021/acs.energyfuels.7b02728.
[56] C. Jian, T. Tang, S. Bhattacharjee, Probing the effect of side-chain length on the aggregation of a model asphaltene using molecular dynamics simulations, Energy Fuels 27 (2013) 2057–2067, https://doi.org/10.1021/ef400097h.
[57] A. Ekramipooya, F.M. Valadi, A. Farisabadi, M.R. Gholami, Effect of the heteroatom presence in different positions of the model asphaltene structure on the self-aggregation: MD and DFT study, J. Mol. Liq. 334 (2021) 116109, https://doi.org/10.1016/j.molliq.2021.116109.
[58] M. Li, Z. Bi, L. Xie, G. Sun, Z. Liu, Q. Kong, X. Wei, C.-M. Chen, From starch to carbon materials: insight into the cross-linking reaction and its influence on the carbonization process, ACS Sustain. Chem. Eng. 7 (2019) 14796–14804, https://doi.org/10.1021/acssuschemeng.9b02821.